

A cosmological hydrodynamic code based on the Piecewise Parabolic Method

Claudio Gheller¹, Ornella Pantano² and Lauro Moscardini³

¹ *SISSA – International School for Advanced Studies, via Beirut 2–4, I–34013 Trieste, Italy*

² *Dipartimento di Fisica Galileo Galilei, Università di Padova, via Marzolo 8, I–35131 Padova, Italy*

³ *Dipartimento di Astronomia, Università di Padova, vicolo dell’Osservatorio 5, I–35122 Padova, Italy*

1 February 2008

ABSTRACT

We present a hydrodynamical code for cosmological simulations which uses the Piecewise Parabolic Method (PPM) to follow the dynamics of gas component and an N–body Particle–Mesh algorithm for the evolution of collisionless component. The gravitational interaction between the two components is regulated by the Poisson equation which is solved by a standard FFT procedure. In order to simulate cosmological flows we have introduced several modifications to the original PPM scheme which we describe in detail. Various tests of the code are presented including adiabatic expansion, single and multiple pancake formation and three-dimensional cosmological simulations with initial conditions based on the cold dark matter scenario.

Key words: Hydrodynamics - Methods: numerical - Large-scale structure of the Universe

1 INTRODUCTION

Most of the present cosmological models are based on the assumption that in the universe two different kinds of matter are present: the baryonic matter, which is directly observed and forms all of the bright objects, from stars to the hot gas present in X–ray clusters, and a dark, collisionless component which accounts for most of the gravitational mass in the Universe. The evolution of this system can only be described by treating both components at the same time, looking at all of their internal processes and considering their mutual interaction. In this way, making a suitable choice of the initial conditions, one can describe the evolution of cosmological structures and estimate all of the related physical observables. This can only be achieved by using numerical simulations which allow a general description of the non–linear evolution of the structures. In particular N–body techniques (Hockney & Eastwood 1981; Efstathiou et al. 1985; Barnes & Hut 1986) have proved to be particularly effective for cosmological problems in which the dynamics is controlled by gravitational forces as in the case of the dark matter and also for baryonic structures on very large scales (more than $50h^{-1}$ Mpc). With these methods matter is described as a set of collisionless particles and its dynamics is governed by the Boltzmann equation.

The N–body approach, however, is not in general suitable for describing the behaviour of the baryonic component which is also influenced by pressure forces, heating and cooling processes. The inclusion of all these phenomena requires an enormous amount of computational resources as they act on a very wide range of scales. The thermal input from gravitationally induced shocks is, for example, maximally effective at about 10 Mpc, while cooling processes are most important on scales less than 0.1 Mpc. Therefore to take into account all of these processes requires a minimum of 10^6 resolution elements in three dimensions. The lack of adequate computational resources has delayed the development of hydrodynamic cosmological codes and only in recent years have a number of numerical schemes been proposed for following the evolution of baryonic matter.

A first family of these techniques derives directly from the N–body methods. It is called “Smoothed Particle Hydrodynamics” (SPH) and represents fundamental fluid elements in terms of particles. The SPH methods are intrinsically Lagrangian and, following the fluid elements in their motion, have high spatial resolution and give an accurate description of high–density regions, where particles tend to concentrate. On the other hand they cannot treat properly low–density regions where few particles are present and mass resolution is poor. For a detailed introduction to these methods we refer to Hernquist & Katz (1989), Evrard (1990) and Steinmetz & Muller (1993).

Recently Gnedin (1995; see also Gnedin & Bertschinger 1996) has presented a new approach to cosmological hydrodynamics called SLH (softened Lagrangian hydrodynamics) which utilizes a high resolution Lagrangian hydrodynamics code combined with a low resolution Eulerian solver. Its properties are intermediate between the Eulerian and SPH approaches.

Multi-dimensional hydrodynamic codes not based on SPH, usually adopt an Eulerian approach and dynamical equations are solved on a fixed (or adaptive) grid. Mean values of the fluid quantities are computed in each grid cell by solving the equations of conservation of matter, momentum and energy density once the equation of state for the matter is given. Eulerian methods have good mass resolution, and can describe low-density regions better than SPH but they are spatially limited by the cell size. An Eulerian approach has been adopted in the majority of the hydrodynamical codes developed for studying large scale structures (Chiang, Ryu & Vishniac 1989; Cen 1992; Ryu et al. 1993; Bryan et al. 1995; Quilis, Ibáñez & Saez 1996; Sornborger et al. 1996). For a comprehensive comparison between the Lagrangian and Eulerian approaches we refer to Kang et al. (1994).

In this paper we describe a cosmological hydrodynamic code that we have developed using the Piecewise Parabolic Method (PPM) introduced by Colella & Woodward (1984). This is a higher order extension of Godunov's shock capturing method (Godunov 1959; 1961). It is at least second-order accurate in space (up to the fourth-order, in the case of smooth flows and small timesteps) and second-order accurate in time. The high accuracy of this method allows minimization of errors due to the finite size of the cells of the grid and leads to a spatial resolution close to the nominal one. In a cosmological framework, the basic PPM technique has to be modified to include the gravitational interaction and the expansion of the universe. In the gravitational collapse of cosmological structures, extremely supersonic flows are generated and so the thermal energy cannot be computed accurately from the total energy, as is usually done. Thermal energy is only a small fraction of the total energy and so negative values or a spurious heating can both be found as a result of numerical errors. This difficulty has been overcome by computing simultaneously the total and the internal energy.

The PPM algorithm has already been used for building a cosmological code by Bryan et al. (1995), however our approach differs in several respects from theirs. In the Bryan et al. work, the one-dimensional time integration is done by first performing a Lagrangian step and then remapping the results onto an Eulerian grid expressed in the usual coordinates comoving with the mean Hubble flow. We instead adopt a single-step Eulerian scheme. The construction of the effective left and right states for the Riemann problem is then more complicated than in the Lagrangian case, since the number of characteristics reaching the edge of a zone is not constant. On the other hand, this choice allows us to include in the characteristic equations both the gravitational interaction and the expansion of the universe and then the effect of all source terms is accounted for to second-order. Moreover, an Eulerian approach seems to be preferable in the case of complicated three-dimensional structures (Colella & Woodward 1984).

The hydrodynamical part has been coupled to a Particle Mesh (PM) N-body code that describes the evolution of the dark component. The standard PM code has been modified to work with a non-constant timestep equal to that used in the hydrodynamical integration. The coupling is obtained by calculating the gravitational field due to both the components by the usual FFT procedure.

The plan of the paper is as follows. In Section 2 we present the basic equations written in comoving coordinates. In Section 3 we describe the basic numerical method and the modifications needed for cosmological calculations. The numerical tests and results from cosmological simulations are presented in Section 4, while conclusions are drawn in Section 5. A more detailed description of the numerical scheme and of the method used for computing the fluxes are presented in the appendices.

2 DYNAMICAL EQUATIONS

The cosmological hydrodynamic equations for a self-gravitating gas in coordinates comoving with the expanding universe are:

$$\frac{\partial \varrho}{\partial t} + \frac{1}{a} \frac{\partial}{\partial x_j} (\varrho v_j) = 0, \quad (1)$$

$$\frac{\partial \varrho v_i}{\partial t} + \frac{1}{a} \frac{\partial}{\partial x_j} (\varrho v_i v_j + p \delta_{i,j}) = -\frac{\dot{a}}{a} \varrho v_i - \frac{1}{a} \varrho \frac{\partial \phi}{\partial x_i}, \quad (2)$$

$$\frac{\partial E}{\partial t} + \frac{1}{a} \frac{\partial}{\partial x_j} [(E + p) v_j] = -2 \frac{\dot{a}}{a} E - \frac{1}{a} \varrho v_j \frac{\partial \phi}{\partial x_j}, \quad (3)$$

where x_j and v_j are the j -th component of the comoving coordinate and of the proper peculiar velocity, respectively; t is the cosmic time; a is the cosmological expansion factor; ϕ is the peculiar gravitational potential; ϱ is the comoving matter density; E is the total energy per unit comoving volume; p is the comoving pressure.

We treat the baryonic matter as an ideal gas with adiabatic index $\gamma = 5/3$ and its equation of state is:

$$p = (\gamma - 1) \left(E - \frac{1}{2} \varrho \mathbf{v}^2 \right). \quad (4)$$

where \mathbf{v}^2 is the square norm of the velocity vector.

The dynamics of collisionless matter is described in comoving coordinates by the following set of equations:

$$\frac{dx_j}{dt} = \frac{1}{a} v_j , \quad (5)$$

$$\frac{dv_j}{dt} + \frac{\dot{a}}{a} v_j = -\frac{1}{a} \frac{\partial \phi}{\partial x_j} . \quad (6)$$

The peculiar gravitational potential is computed by solving the Poisson equation:

$$\nabla^2 \phi = \frac{4\pi G}{a} (\varrho_{tot} - \varrho_0) , \quad (7)$$

where ϱ_{tot} is the total comoving density (baryonic plus dark matter) and ϱ_0 is the comoving mean density.

In the code we have normalized the variables using as basic units the final time t_0 , the comoving cell size x_0 and the comoving mean density ϱ_0 at time t_0 . The expansion factor at the final time is set as $a_0 = 1$. The other variables are normalized as follows: $v_j/(x_0/t_0)$, $E/(\varrho_0 x_0^2/t_0^2)$, $p/(\varrho_0 x_0^2/t_0^2)$ and $\phi/(x_0^2/t_0^2)$.

The physical temperature T is related to the previous normalized quantities by

$$T = \frac{m_p}{K_B} \left(\frac{x_0}{t_0} \right)^2 \frac{p}{\varrho} , \quad (8)$$

where K_B is Boltzmann's constant and m_p is the proton mass.

3 CODE STRUCTURE

3.1 The PPM Scheme

The choice of the PPM scheme for the integration of hydrodynamical equations has been suggested by the particular problems which one has to face in a cosmological computation. The presence of highly supersonic flows and the formation of strong shocks during the collapse of structures require a very accurate treatment. Moreover the description of phenomena which act simultaneously on a very wide range of scales needs as much resolution as possible with a given number of cells.

The PPM algorithm, developed by Colella & Woodward (1984), belongs to a class of schemes in which an accurate representation of flow discontinuities is made possible by building into the numerical method the calculation of the propagation and interaction of non-linear waves. There are two possible formulations of the PPM scheme: hydrodynamical equations can be solved either in a single Eulerian step or with a Lagrangian step followed by a remapping onto the Eulerian grid. We have adopted the first approach as it appears more suitable for problems with complicated spatially dependent source terms. A detailed presentation of the finite difference equations used in the code are presented in Appendices A1 and A2: here we describe the basic operations characterizing the PPM scheme.

In the PPM method we start from the knowledge of a set of zone-averaged values of hydrodynamical quantities. To update these averages we solve hydrodynamical conservation equations: this requires the estimate of the fluxes of the conserved quantities at the zone interfaces which is done according to the following one-dimensional procedure. First, we construct a piecewise parabolic (third-order) one-dimensional interpolation function for each of the hydrodynamical variables and for the source terms. This leads to a more accurate representation of smooth spatial gradients as well as a sharper description of discontinuities. The interpolation polynomial w is computed such that:

$$w_j = \frac{1}{\Delta x} \int_{x_{j-1/2}}^{x_{j+1/2}} w(\xi) d\xi , \quad (9)$$

where w_j is the mean value of the interpolation polynomial over the j -th zone, $x_{j\pm 1/2}$ are the positions of the zone interfaces and $\Delta x = x_{j+1/2} - x_{j-1/2}$. It is also required that inside each zone $w(\xi)$ is continuous and monotonic.

The interpolated distributions can then be used to estimate properly the average values of the variables to the left and right of each zone edge. This is performed in two steps. In the first step, one determines the characteristic domain of dependence with respect to a zone edge, that is the regions of space to the left and to the right of the edge that contain all of the information that can reach the zone edge during the current timestep. Then, using the interpolated distributions, the mean values of hydrodynamic variables are computed over the domains of dependence on each side of the edge. In the second step, we solve the Riemann problem using as initial left and right states the mean values of hydrodynamical variables computed previously on each side of the zone edge. The solution of this gives the time averaged values of the variables at the zone edge which are then used to compute inter-cell fluxes and hence the fluid variables at the new time. This closes the basic one-dimensional PPM loop.

The extension to more dimensions is achieved using a direction splitting procedure (Strang 1968). If we indicate with L_k the integration in the k -th direction, the updated value for the generic hydrodynamical variable u is

$$u^{new} = L_z L_y L_x u^{old} . \quad (10)$$

In order to preserve second-order accuracy in space, in successive timestep the order of directional integration is permuted as follows:

$$L_z L_y L_x, L_x L_y L_z, L_x L_z L_y, L_y L_z L_x, L_y L_x L_z, L_z L_x L_y . \quad (11)$$

For cosmological applications several important modifications must be introduced into the basic PPM scheme. The inclusion of gravitational forces and cosmic expansion changes the form of the usual hydrodynamical equations. Expansion of the universe enters the hydrodynamical equations in two different ways. First, all of the fluxes and the source terms are multiplied by the factor $1/a(t)$. Second, two further terms appear: $(\dot{a}/a)\varrho v_j$ and $(\dot{a}/a)E$ in the equations for conservation of momentum and energy, respectively (in the following we will refer to these terms as expansion terms). This leads to important changes both in the Riemann solver, as we will show in the next section, and in the final integration. In this last step, forces and expansion terms are treated in different ways. First hydrodynamical quantities are updated without considering the expansion terms. These in fact, being proportional to the integrated quantity itself, cannot be included in the basic integration procedure. The time centered values of gravitational forces are calculated by finite differencing the potential field computed by linear extrapolation at $t^{n+1/2}$. In order to obtain a proper estimate of the force felt by a fluid element, its averaged value over the entire zone is calculated. Finally, we compute the effect of expansion terms by using a semi-implicit scheme (see equations A8-A10 and A17).

3.2 Characteristic Equations

The solution of the Riemann problem, which is the central feature of the Godunov approach, requires knowledge of the characteristic form of hydrodynamic equations. Because of our choice of coordinates comoving with the expanding universe, the finite difference expressions which we use in the Riemann solver differ slightly from those discussed in Woodward & Colella (1984). In this section we write the characteristic equations for the system (1)–(3), while in Appendix A2 we present the scheme used in the code for computing hydrodynamic fluxes.

For the time integration we use a directional splitting procedure. Indicating by x the relevant space direction during the one-dimensional sweep, by v the velocity in the direction of the one-dimensional sweep and by u the velocity orthogonal to v , equations (1)–(3) can be rewritten in the following non-conservative form:

$$\frac{\partial \mathbf{U}}{\partial t} + \mathcal{A} \frac{\partial \mathbf{U}}{\partial x} + \mathbf{C} = 0 , \quad (12)$$

where

$$\mathbf{U} = \begin{pmatrix} \varrho \\ v \\ u \\ p \end{pmatrix} , \quad \mathcal{A} = \frac{1}{a} \begin{pmatrix} v & 0 & 0 & \varrho \\ 0 & v & 0 & 1/\varrho \\ 0 & 0 & v & 0 \\ 0 & \gamma p & 0 & v \end{pmatrix} , \quad \mathbf{C} = \begin{pmatrix} 0 \\ v\dot{a}/a - g \\ u\dot{a}/a \\ 2p\dot{a}/a \end{pmatrix} . \quad (13)$$

In order to find the characteristic form of this system, we first solve the corresponding eigenvalue equation:

$$\det(\mathcal{A} - \lambda \mathcal{I}) = 0 \quad (14)$$

obtaining as eigenvalues:

$$\lambda_0 = \frac{v}{a} , \quad \lambda_- = \frac{v-c}{a} , \quad \lambda_+ = \frac{v+c}{a} , \quad (15)$$

where λ_0 is a double solution and c is the sound speed. The eigenvalues are used to compute the domain of dependence of a given fluid element. Note that in expanding coordinates the domain must be rescaled by the factor $a(t)$ with respect to that for a non-expanding system.

The corresponding left eigenvectors \mathbf{l}_k are:

$$\mathbf{l}_{01} = (0, 0, 1, 0) \quad (16)$$

$$\mathbf{l}_{02} = (1, 0, 0, -1/c^2) \quad (17)$$

$$\mathbf{l}_- = (0, -\frac{\varrho c}{2}, 0, \frac{1}{2}) \quad (18)$$

$$\mathbf{l}_+ = (0, \frac{\varrho c}{2}, 0, \frac{1}{2}) . \quad (19)$$

The characteristic form of hydrodynamical equations is then:

$$\mathbf{l}_k \frac{\partial \mathbf{U}}{\partial t} + \mathbf{l}_k \mathcal{A} \frac{\partial \mathbf{U}}{\partial x} + \mathbf{l}_k \mathbf{C} dt = 0 , \quad (20)$$

$$\mathbf{l}_k \frac{\partial \mathbf{U}}{\partial t} + \lambda_k \mathbf{l}_k \frac{\partial \mathbf{U}}{\partial x} + \mathbf{l}_k \mathbf{C} dt = 0 , \quad (21)$$

that is:

$$\mathbf{l}_k d\mathbf{U} + \mathbf{l}_k \mathbf{C} dt = 0, \quad \text{along } \frac{dx}{dt} = \lambda_k. \quad (22)$$

For our fluid, the characteristic equations are:

$$c^2 d\rho - dp - 2\frac{\dot{a}}{a}p dt = 0 \quad (23)$$

$$du - \frac{\dot{a}}{a}u dt = 0 \quad (24)$$

along $dx/dt = v/a$, and

$$dp \pm \rho c dv + \left[2\frac{\dot{a}}{a}p \pm \rho c \left(\frac{\dot{a}}{a}v - g \right) \right] dt = 0 \quad (25)$$

along $dx/dt = (v \pm c)/a$.

Characteristic equations are used both for calculating the domain of dependence of a zone edge and in the construction of the Riemann solver where we take account, to second-order, of the gravity and expansion (see Appendix A2). The solution of the Riemann problem gives the required time-averaged values of the hydrodynamical variables which are used in the final integration step.

3.3 Correction to the Energy

In order for overall energy to be accurately conserved it is important to use the total energy density E directly as a dependent variable (see equation 3) rather than calculate it as the sum of the kinetic and internal energy densities ($\frac{1}{2}\rho\mathbf{v}^2$ and e , respectively). The value of e is however required in order to calculate the thermodynamic quantities such as pressure and temperature and the original PPM code calculates e as the difference between E and $\frac{1}{2}\rho\mathbf{v}^2$. However, there is a problem with this for cosmological simulations where highly supersonic flows are often present. In these situations, the ratio between the kinetic and internal energies can reach values up to 10^8 in which case the errors in calculating e by the standard PPM procedure become much larger than the quantity itself.

In our code, we solved this problem by calculating both the total and internal energy per unit comoving volume. In comoving coordinates the equation for the internal energy density $e = p/(\gamma - 1)$ is the following:

$$\frac{\partial e}{\partial t} = -\frac{1}{a} \frac{\partial}{\partial x_k} (ev_k) - 2\frac{\dot{a}}{a}e - \frac{1}{a}p \frac{\partial v_k}{\partial x_k}. \quad (26)$$

Hence, at each timestep, both the total and internal energy equations are solved and the results combined according to the local conditions in the fluid. The value obtained from equation (26) has to be only used when the internal energy cannot be calculated correctly as the difference between total and kinetic energy. This is usually the case in expanding or weakly compressing (comoving) regions, that is in regions in which one of the following conditions holds:

$$\nabla \cdot \mathbf{v} \geq 0, \quad \frac{1}{p} |\nabla p| \leq \eta_1. \quad (27)$$

If neither of these conditions is verified, the internal energy is computed according to the following criterion:

$$e = \begin{cases} E - \frac{1}{2}\rho\mathbf{v}^2 & \text{if } E - \frac{1}{2}\rho\mathbf{v}^2/E \geq \eta_2 \\ e & \text{otherwise,} \end{cases} \quad (28)$$

where η_1 and η_2 are suitable parameters smaller than unity, fixed on the bases of numerical experimentation. Various tests have suggested the use of the following values: $\eta_1 = 0.3$ and $\eta_2 = 0.005$.

3.4 N-body Code

The dynamics of the dark component is described using a PM N-body code (Hockney & Eastwood 1981). In order to solve equations (5)–(6) the standard second-order leapfrog method has been replaced by a second-order two-step Lax–Wendroff method (see Appendix A1). The leapfrog scheme requires a constant timestep, while hydrodynamics makes it desirable to have a variable time interval. Density and forces are calculated by using the cloud-in-cell interpolation scheme.

3.5 Timestep

In determining the new timestep at the end of each loop we impose several constraints. First of all, we require that the maximum variation of the expansion factor a during a timestep is less than 2%. We impose also that dark matter particles move no more than half a cell in a single step and that the baryonic dynamics satisfies the Courant condition:

$$\Delta t \leq \min \left[\frac{C_c a(t) \Delta x}{[c + \max(|v_x|, |v_y|, |v_z|)]} \right], \quad (29)$$

where C_c is the Courant number and the minimum is computed over all cells. We set $C_c = 0.5$. Finally, we require that in a single step the timestep increases by no more than 20% from its previous value.

Our tests indicate that the expansion condition is important only in the first part of the simulation, when the amplitude of the fluctuations is still small. At later times the Courant condition becomes the dominant one.

4 TESTS OF THE CODE

Our code has been subjected to a series of numerical tests, ranging from the purely hydrodynamical to cosmological ones, in one and more dimensions. In each case conservation of energy has been checked. For the cosmological tests this check has been performed by using the cosmic energy equation which for an ideal gas in an expanding frame is (Peebles 1980):

$$\frac{d}{dt}(E + W) + \frac{\dot{a}}{a}(2E + W) = 0, \quad (30)$$

where E is the total (internal plus kinetic) comoving energy and W is the gravitational energy of the gas.

Equation (30) can be rewritten as:

$$\frac{d}{dt}[a(E + W)] + \dot{a}E = 0 \quad (31)$$

and integrated with respect to the expansion factor giving:

$$a_2 E(a_2) - a_1 E(a_1) + \int_{a_1}^{a_2} E da = -[a_2 W(a_2) - a_1 W(a_1)], \quad (32)$$

where a_1 and a_2 are the values of the expansion factor at two different times.

We checked energy conservation computing the quantity:

$$R = \frac{a_2 E(a_2) - a_1 E(a_1) + \int_{a_1}^{a_2} E da}{-[a_2 W(a_2) - a_1 W(a_1)]}. \quad (33)$$

For perfect energy conservation R should remain as unity. The results obtained in our tests are presented in the following subsections.

4.1 One-Dimensional Shock Tube Test

In Fig. 1 we present the results of a standard shock tube test. In this case we solve the hydrodynamical equations (1)–(3) without the source terms on the right hand side and with $a = 1$. Initially the gas is at rest ($v = 0$) and density and pressure show a central jump from $\varrho_l = 1$, $p_l = 1$ to $\varrho_r = 0.1$, $p_r = 0.1$. The calculation is performed using a grid of 128 zones, the initial time is $t_i = 1$ and the final time, shown in the figure, is $t_0 = 20$.

The numerical results (open circles) are in very good agreement with the analytical ones (solid lines). In particular, shocks are typically resolved within one cell and contact discontinuities are represented in four or five zones. In order to reduce the diffusion of contacts we have used, for the density field, the discontinuity detection algorithm of Colella & Woodward (1984). We have not introduced artificial diffusion and/or numerical flattening since numerical ripples around steep gradients are either absent or very small and do not affect the solution during the whole evolution.

4.2 Adiabatic Expansion

After having tested the hydrodynamic part of the code alone, we have introduced expansion and gravity and have concentrated on tests describing physical situations that are expected in cosmological simulations. In all of the following tests we have assumed an Einstein–de Sitter pure baryonic universe with vanishing cosmological constant and we fixed the value $H_0 = 50 \text{ km s}^{-1} \text{ Mpc}^{-1}$ for the Hubble constant. The comoving size of the computational box is $L = 64 h^{-1} \text{ Mpc}$. For this model our basic units of normalization are:

$$\varrho_0 = \frac{3H_0^2}{8\pi G} \quad t_0 = \frac{1}{(6\pi G \varrho_0)^{1/2}}, \quad (34)$$

where G is the gravitational constant. The expansion factor depends on the cosmological time as

$$a(t) \propto t^{2/3}. \quad (35)$$

As a first test we have simulated the adiabatic expansion of an unperturbed universe, starting at time $t_i = 0.01$ from a homogenous distribution of matter with velocity $v_i = 100 \text{ km s}^{-1}$ and temperature $T_i = 4.6 \text{ K}$. In this situation equations (2)–(3) are easily integrated giving:

$$v = v_i(a_i/a), \quad T = T_i(a_i/a)^2, \quad (36)$$

where a , v and T are the expansion factor, the velocity and the temperature respectively, at time t . At the final time $t_0 = 1$ numerical and analytical solutions are compared and the errors calculated as:

$$\Delta T = \frac{|T_{num} - T_{an}|}{T_{an}}, \quad \Delta v = \frac{|v_{num} - v_{an}|}{v_{an}}, \quad (37)$$

where the subscripts *num* and *an* indicate, respectively, the numerical and analytical values of the variables. We have indicated with Δa the maximum fractional variation of the expansion factor in a timestep. Using $\Delta a = 0.1$ we have obtained $\Delta T = 6 \times 10^{-3}$ and $\Delta v = 3 \times 10^{-3}$. The errors decrease to $\Delta T = 8 \times 10^{-5}$ and $\Delta v = 4 \times 10^{-5}$ for $\Delta a = 0.01$. The value of the parameter Δa used in the simulations is fixed by considering the balance between accuracy and computational time.

4.3 Zel’dovich Pancake

In this test we describe the formation of a one-dimensional pancake. The test is particularly important for cosmological studies as all of the related physics (hydrodynamics, expansion, gravity) is included. In addition, it represents the evolution of an initial sinusoidal wave and so can be seen as a single-mode analysis of the full three-dimensional problem.

At the initial time, corresponding to $a_i = 0.01$, a sinusoidal velocity field has been imposed on the computational grid. The amplitude of the initial perturbation has been chosen such that the caustic forms at $a_c = 0.5$. At a_i the density and temperature fields are uniform. We set $\varrho = 1$ and $T = 100 \text{ K}$. The final time corresponds to $a_0 = 1$. The same test has been repeated using eight different numbers of zones ranging from $N_c = 8$ to $N_c = 1024$.

During the first part of the evolution, we are in the linear phase and the numerical results can be directly compared with the analytical solution which applies for a non-collisional fluid since the effect of the pressure is negligible in this phase. This comparison gives an estimate of the accuracy of the code. Moreover, using results obtained with different numbers of zones we can study the convergence of the numerical solution. The error is computed as:

$$\Delta \varrho = \frac{1}{N_g} \sum_{i=1}^{N_g} \frac{|\varrho(x_i) - \varrho_e(x_i)|}{\varrho_e(x_i)}, \quad (38)$$

where ϱ_e is the exact solution. We found that at $a \sim 0.1$, when shocks are not present, the error is below 1% already with only 16 zones.

The non-linear phase of the evolution is the most interesting. The strong shocks and large gradients that form are in fact a severe test for any Eulerian numerical code. The results at $a_0 = 1$ obtained using grids of 256 and 1024 zones are compared in Fig. 2. The only important difference between the two solutions is the height of the central density peak, but this was expected as a consequence of the different resolutions in the two cases. All of the other features the solution are in very good agreement between the two simulations showing the convergence of the numerical solution. Shocks are resolved in one zone and there are no numerical postshock ripples.

In Fig. 3 we present the results of the energy conservation test. We have calculated at the final time the conservation parameter R (defined in equation 33) and the total gravitational (W), kinetic (E_{KIN}) and thermal (E_{TH}) energy of the fluid when a various number of cells N_c are adopted. The energy is plotted in the code units. The error in the energy conservation is of about 5% for $N_c = 32$ and decreases to 0.1% for $N_c = 1024$. The behaviour of the three energy terms shows that at least 32 zones are needed for starting to see the convergence of the solution. The poor resolution of the 8 and 16 zone cases, in fact, makes it impossible to describe correctly the narrow central peak, which remains too diffused. The shallower central potential wells induce a smaller acceleration in the infalling matter. The compression is low and the transformation from kinetic to internal energy is inefficient and so produces a pressure which is too low to support the infall of the matter. However the collapse of the peak is prevented by the artificial effect of the coarseness of the grid.

4.4 Multiple Pancake Formation.

The last one-dimensional test which we have performed consists of simulating the evolution of a random initial density field. In this test different wavelengths evolve together; hence we can verify the ability of the code for describing shock interactions and the merging of small structures.

The initial conditions are set by perturbing the density field according to a Gaussian random distribution characterized by a power-law spectrum of the general form

$$P(k) = P_0 k^n \exp(-k^2 R_f^2), \quad (39)$$

where P_0 is the normalization constant and n is the spectral index. The short wavelength cut-off at the scale $R_f = 2$ grid-points ensures that the results are not affected by the sampling of modes whose size is close to that of the resolution of the simulation.

The normalization constant is fixed requiring that the one-dimensional variance σ^2 at the final time t_0 (corresponding to the expansion factor $a_0 = 1$) for linearly evolved perturbations is equal to unity on the scale $R_* = 10^{-1}L$ so that:

$$\sigma^2(R_*) = \frac{1}{\pi} \int_0^\infty P(k)W(kR_*) dk = 1, \quad (40)$$

where the function $W(kR_*)$ is a one-dimensional top-hat filter:

$$W(kR_*) = \frac{\sin(kR_*)}{kR_*}. \quad (41)$$

The initial time t_i is chosen by imposing that, at t_i , the largest density fluctuation is equal to unity, so that the system can be considered still evolving linearly.

As an example, we show in Fig. 4 the results at the final time t_0 for a simulation with spectral index $n = 1$ when $N_c = 256$ is used, i.e. with the same number of cells used in the simulation of the single pancake. Shocked regions, characterized by the presence of typical double peaked maxima in the temperature field and by the smoothing of steep negative gradients in the velocity field, are at temperatures ranging from 10^4 to 10^6 K. Underdense regions are instead at much lower temperature. Collapsing regions surrounding density peaks are, at the beginning, at low temperature, but heat up as soon as propagating shocks reach them. The errors in energy conservation are around 3%, slightly higher than the value obtained for the Zel'dovich pancake test.

The different clustering properties of baryonic and dark matter and the multiple pancake formation have been studied in much more detail in Gheller, Moscardini & Pantano (1996) by using numerical simulations based on a one-dimensional version of the PPM+PM code presented here. In that paper power-law initial power spectra with $-1 \leq n \leq 3$ have been simulated using 8192 zones and 16384 particles. The results show that at large scales the final distribution of the two components is very similar while at small scales the dark matter presents a lumpiness which is not found in the baryonic matter.

4.5 Cold Dark Matter Universe

As first checks of our complete fully three-dimensional code, we repeated the tests of the one-dimensional shock tube and of the Zel'dovich pancake formation. Using a 64^3 grid, the results (not shown here) are consistent with those obtained with a similar resolution in one-dimension. Finally we have simulated the evolution of a purely baryonic Einstein-de Sitter Universe with an initial cold dark matter (CDM) power spectrum. As in the previous tests, we fixed the Hubble constant to be $H_0 = 50 \text{ km s}^{-1} \text{ Mpc}^{-1}$ and the comoving size of the computational box to be $L = 64 \text{ h}^{-1} \text{ Mpc}$. In this way our numerical results can be compared with those obtained by Kang et al. (1994), even if a different random realization of the initial conditions has been used. Perturbations are initially Gaussian distributed and the primordial density power spectrum can be written in the form:

$$P(k) = P_0 k^n T^2(k), \quad (42)$$

where $T(k)$ is the CDM transfer function given by the Davis et al. (1985) fitting formula:

$$T(k) = (1 + 6.8k + 72.0k^{3/2} + 16.0k^2)^{-1}. \quad (43)$$

In the standard CDM model, the primordial spectral index has the Zel'dovich value $n = 1$.

The normalization constant P_0 is fixed such that the linear mass variance at the present time is unity in a sharp-edged sphere of radius $R_8 = 8h^{-1} \text{ Mpc}$:

$$\sigma^2(R_8) = \frac{P_0}{2\pi^2} \int_0^\infty k^{n+2} T^2(k) W_{TH}^2(kR_8) dk = 1. \quad (44)$$

In the above equation, $W_{TH}(kR) = (3/kR)j_l(kR)$ is a top-hat window function and j_l denotes the l th-order spherical Bessel function. The velocity field at the initial time t_i has been calculated in the linear perturbation approximation (Peebles 1980) as:

$$\mathbf{v} = \frac{2 \nabla \Phi}{3H(t_i)a(t_i)}. \quad (45)$$

We are interested in checking the convergence properties of our code, so we evolved the same initial conditions on three different grids with 32^3 , 64^3 and 128^3 cells, respectively. The initial conditions are set up according to the previous prescriptions on the coarsest grid. The initial time, fixed by the condition that the maximum density fluctuation is unity, corresponds to a redshift $z \sim 20$. We run our simulations on a IBM RISC 6000/590.

We have first analyzed some integral properties of the results at the final time. We have calculated the mean temperature $\langle T \rangle$, the average mean temperature $\langle T \rangle_\varrho \equiv \langle T \varrho \rangle / \langle \varrho \rangle$, the average temperature weighted by the density squared $\langle T \rangle_{\varrho^2} \equiv$

[tp]

Table 1. The simulations. Column 1: the number of zones in each dimension N_c ; Column 2: the mean temperature $\langle T \rangle$. Column 3: the average mean temperature $\langle T \rangle_\varrho$. Column 4: the average temperature weighted by the density squared $\langle T \rangle_{\varrho^2}$. Column 5: the r.m.s. of the density fluctuation field σ .

N_c	$\langle T \rangle$	$\langle T \rangle_\varrho$	$\langle T \rangle_{\varrho^2}$	σ
32	1.48	6.02	19.49	2.17
64	2.02	10.61	28.63	2.48
128	2.02	11.91	32.95	2.77

$\langle T \varrho^2 \rangle / \langle \varrho^2 \rangle$ and the variance of the density fluctuation field $\sigma^2 \equiv (\langle \varrho^2 \rangle / \langle \varrho \rangle^2 - 1)$. As in Kang et al. (1994), the calculation has been performed for the data rebinned to a 16^3 grid. The results are presented in Table 1.

The average temperature for the rebinned data seems to have converged already in the 64^3 simulation. However, the behaviour of the rms density fluctuation suggests that a higher resolution is needed for the convergence of the density field. The variation of the density weighted temperatures between the 64^3 and 128^3 grids depends essentially on variations of density distribution. As already noticed by Kang et al. (1994) for all the eulerian codes considered in that paper, the values of σ appear to converge from below.

In Fig. 5 we show a cell-by-cell comparison of density and temperature for the rebinned data of the three simulations. We always observe a good correlation between the values of the densities obtained from simulations with different resolutions; the spread of the points is reduced as we compare simulations with the highest resolution. The same holds for the high temperature cells. The distribution at lower temperatures is due to the formation of substructures as we increase the grid resolution. The large number of points which accumulate in the lower part of the panel represents cells that in the lower resolution simulation are cooling according to the expansion of the Universe while in the higher resolution run are site of some structure. Also this effect decreases when the resolution is higher.

In the left and right columns of Fig. 6 we show the volume and mass weighted density histograms, $f(N)$ and $f(M)$ respectively, for the 16^3 rebinned data. The tendency to form higher density peaks as we increase the resolution clearly appears in these histograms. As we go from 32^3 to 128^3 the amount of mass contained in the high density regions increases. However, in relation to the convergence of the numerical results, it is encouraging to see that the density distribution both in volume and in mass is very similar for the 64^3 and 128^3 runs.

The corresponding histograms for the temperature are shown in Fig. 7. Comparing the rebinned data from different runs we can observe higher gas temperatures when the resolution of the simulation is increased. We notice both an increase in volume fraction and in mass fraction of the gas at high temperature. The $f(N)$ peak at low temperature is almost absent in the 128^3 simulation, but this is only due to the averaging procedure in constructing the rebinned data. Small scale structures are present in the high resolution run which could not appear in the simulations with a smaller number of cells and they have the effect of raising the average temperature in the rebinned data.

The same effect is evident if we look at Fig. 8 which presents the same histograms for the original data of the 128^3 simulation: a large fraction of the volume is still at low temperature. However, the mass fraction distribution confirms that about 70% of the mass is at temperatures higher than 10^6 K.

In Fig. 9 we show two different slices of the simulation with $0.5 h^{-1}$ Mpc thickness (1 cell). For each slice contour plots are presented for the density contrast $\delta = \varrho / \langle \varrho \rangle - 1$ and the temperature. Structures appear well resolved and strong temperature gradients indicate shock positions. High density peaks are surrounded by high temperature regions which have been heated by the shock propagation.

Finally in Fig. 10 the contour plots of the volume (left) and mass (right) fraction with given temperature and density are shown. We observe that most of gas is at high density and temperature. On the other hand most of the volume is at low density with either high or low temperatures depending on whether it has been crossed by shocks or not.

5 CONCLUSIONS

We have presented a new numerical code developed for studying the formation and evolution of cosmological structures in both baryonic and dark components. Collisional matter is treated as a fluid and the corresponding hydrodynamic equations are solved using the PPM scheme on a fixed Eulerian grid. We have described the changes to the basic method required by the cosmological applications. Particular care has been taken in including expansion and gravity in the Riemann solver and in the final integration step. This has required the calculation of the characteristic form of the hydrodynamic equations in expanding coordinates. A double formulation of the energy equation has allowed a proper treatment of the highly supersonic

flows common in cosmological simulations. The behaviour of the dark matter is described using a standard Particle Mesh N-body technique, modified to allow the use of a variable timestep, as desirable for hydrodynamics. The two components are coupled through the gravitational interaction and the gravitational field is calculated from the Poisson equation using an FFT procedure.

We have presented a series of tests selected for their relevance in cosmological applications, paying attention both to the accuracy of the highest resolution results and to the convergence of the method when lower resolutions are used.

The one-dimensional tests show that the code can reproduce properly the expected solutions, even when very low resolution is adopted. In particular we present the results of the shock tube test and of single and multiple pancake formation. The CDM test results can be compared with those presented by Ryu et al. (1994), Kang et al. (1994) and Gnedin (1995) showing a good agreement. All of these tests have demonstrated that our code can be considered a reliable and useful tool for cosmological studies.

ACKNOWLEDGMENTS

We would like to thank John Miller for many helpful discussions and comments. This work was partially supported by Italian MURST.

REFERENCES

- Barnes J., Hut P., 1986, *Nat*, 324, 446
 Bryan G.L., Norman M.L., Stone J.M., Cen R.Y., Ostriker J.P., 1995, *Comput. Phys. Comm.*, 89, 149
 Cen R., 1992, *ApJS*, 78, 341
 Chiang W., Ryu D., Vishniac E.T., 1989, *ApJ*, 339, 603
 Colella P., Woodward P., 1984, *J. Comput. Phys.*, 54, 174
 Davis M., Efstathiou G., Frenk C.S., White S.D.M., 1985, *ApJ*, 292, 371
 Efstathiou G., Davis M., Frenk C.S., White S.D.M., 1985, *ApJS*, 57, 241
 Evrard A.E., 1990, *ApJ*, 363, 349
 Gheller C., Moscardini L., Pantano O., 1996, *MNRAS*, 283, 1184
 Gnedin N.Y., 1995, *ApJS*, 97, 231
 Gnedin N.Y., Bertschinger E., 1996, *ApJ*, 470, 115
 Godunov S.K., 1959, *Mat. Sb.*, 47, 271
 Godunov S.K., Zabrodin A.V., Prokopov G.P., 1961, *U.S.S.R Computational Math. and Math. Phys.*, 1, 1187
 Gottlieb J.J., Groth C.P.T., 1988, *J. Comput. Phys.*, 78, 437
 Hernquist L., Katz N.S., 1989, *ApJS*, 64, 715
 Hockney R.W., Eastwood J.W., 1981, *Computer Simulations Using Particles*. McGraw-Hill, New York
 Kang H., Ostriker J.P., Cen R., Ryu D., Hernquist L., Evrard A.E., Bryan G.L., Norman M.L., 1994, *ApJ*, 430, 83
 Peebles P.J.E., 1980, *The Large-Scale Structure of the Universe*. Princeton University Press, Princeton
 Quilis V., Ibáñez J.M., Saez D., 1996, *ApJ*, 469, 11
 Ryu D., Ostriker J.P., Kang H., Cen R., 1993, *ApJ*, 414, 1
 Sornborger A., Fryxell B., Olson K., MacNeice P., 1996, preprint astro-ph/9608019
 Steinmetz M., Muller E., 1993, *A&A*, 268, 391
 Strang G., 1968, *SIAM J. Num. Anal.*, 5, 506
 Van Leer B., 1979, *J. Comput. Phys.*, 32, 101
 Woodward P., Colella P., 1984, *J. Comput. Phys.*, 54, 115

FIGURE CAPTIONS

Figure 1. The velocity v , the pressure p and the density ρ for the one-dimensional shock tube test at the final time $t_0 = 20$. The numerical result obtained with a grid of 128 zones (open circles) is compared to the analytical solution (solid line).

Figure 2. The velocity v , the temperature T and the density ρ for the one-dimensional Zel'dovich pancake test at the final time $a_0 = 1$. The results obtained with grids of 256 (open circles) and 1024 zones (solid line) are compared.

Figure 3. The energy conservation parameter R (top left), the gravitational energy W (top right), the kinetic energy E_{KIN} (down left) and the thermal energy E_{TH} (down right) for the one-dimensional Zel'dovich pancake test are plotted as function of the number of cells N_c .

Figure 4. The velocity v , the temperature T and the density ρ for the one-dimensional multiple pancake test at the final time $a_0 = 1$. A primordial power-law power spectrum with spectral index $n = 1$ is simulated using a grid of 256 zones.

Figure 5. A cell-by-cell comparison of density ρ (upper row) and temperature T (lower row) for the 16^3 rebinned data at $z = 0$ for three simulations with the same initial conditions but different numbers of zones, as indicated by the subscripts.

Figure 6. The volume-weighted $f(N)$ (left column) and mass-weighted $f(M)$ (right column) histograms at $z = 0$ for the density ϱ at $z = 0$ for the 16^3 rebinned data. The results obtained with different numbers of zones are shown: $N_c = 32$ (upper row), $N_c = 64$ (central row) and $N_c = 128$ (lower row).

Figure 7. The same as Fig. 6 but for the temperature T .

Figure 8. The volume-weighted $f(N)$ (upper panels) and mass-weighted $f(M)$ histograms (lower panels) for density ϱ (left column) and temperature T (right column) at $z = 0$ for the original unbinned data of the 128^3 simulation.

Figure 9. Density (left column) and temperature (right column) contour plots of two different slices of $0.5 h^{-1}$ Mpc thickness in the 128^3 run are shown. Density is normalized to the mean density while the temperature is in units of 10^6 K. The density contour levels correspond to $10^{(i-3)/4}$, while the temperature levels are $5^{i/2}$ (solid lines) and 5^{-2i} (dashed lines), where $i = 1, 2, \dots$

Figure 10. Contour plots of the volume fraction (left) and mass fraction (right) with given temperature and density. The results at $z = 0$ from the 128^3 simulation are shown. Contour levels correspond to $10^{i/4}$, where $i = 1, 2, \dots$

APPENDIX A: NUMERICAL SCHEME

We here describe the main steps in the integration of the dynamical equations presented in the text. We used a modified PPM scheme to follow the evolution of baryonic matter and a PM N-body method for the dark matter. The same grid of constant mesh size Δx is used for solving the hydrodynamical equations and for computing the total gravitational potential. The subscript j indicates zone centred values of grid quantities, while subscript $(j + 1/2)$ refers to values computed at the boundary between the j -th and $(j + 1)$ -th zones. Finally, in the dynamical equations for the dark matter the subscript j refers to the j -th particle. Superscripts indicate the time level at which variables are calculated. The same time interval $\Delta t^{n+1/2} = t^{n+1} - t^n$ is used for integrating the dynamical equations of both components. The time-integration of the N-body dynamical equations is performed by a Lax-Wendroff scheme instead of the usual leapfrog scheme which would require a constant timestep.

The main steps in the integration of the dynamical equations are the following:

1 – At the time t^n we have $\varrho_{BM,j}^n$, $\mathbf{v}_{BM,j}^n$ and p_j^n for the baryonic matter. For the dark matter we have $\mathbf{x}_{DM,j}^n$ and $\mathbf{v}_{DM,j}^n$. First we calculate the dark matter density $\varrho_{DM,j}^n$ using a cloud-in-cell mass assignment scheme. Then we compute the total peculiar gravitational potential ϕ_j^n on the grid by solving the Poisson equation using a standard FFT technique. We also extrapolate the gravitational potential to $t^{n+1/2}$ using the values at t^n and t^{n-1}

$$\phi^{n+1/2} = \phi^n \left(1 + \frac{\Delta t^{n+1/2}}{2\Delta t^{n-1/2}} \right) - \phi^{n-1} \frac{\Delta t^{n+1/2}}{2\Delta t^{n-1}}. \quad (\text{A1})$$

2 – We start the hydrodynamical one-dimensional sweep. For a given direction we indicate by v the component of the velocity along the direction of integration and by u the component orthogonal to v . We then calculate the time averaged values of the hydrodynamical quantities at the zone interfaces $\bar{\varrho}_{j+1/2}$, $\bar{p}_{j+1/2}$, $\bar{v}_{j+1/2}$ and $\bar{u}_{j+1/2}$ using the PPM scheme, as described in Section 3.1, 3.2 and in Appendix A2.

3 – We use the time averaged estimates calculated in point 2 to solve the one-dimensional hydrodynamical equations without the inclusion of the expansion terms (for simplicity in the following equations we have dropped the BM subscript):

$$\varrho_{H,j}^{n+1} = \varrho_j^n + \frac{\Delta t^{n+1/2}}{a^{n+1/2}} \left(\frac{\bar{\varrho}_{j-1/2}\bar{v}_{j-1/2} - \bar{\varrho}_{j+1/2}\bar{v}_{j+1/2}}{\Delta x} \right) \quad (\text{A2})$$

$$v_{H,j}^{n+1} = \frac{1}{\varrho_{H,j}^{n+1}} \left[\varrho_j^n v_j^n + \frac{\Delta t^{n+1/2}}{a^{n+1/2}} \left(\frac{\bar{\varrho}_{j-1/2}\bar{v}_{j-1/2}^2 + \bar{p}_{j-1/2} - \bar{\varrho}_{j+1/2}\bar{v}_{j+1/2}^2 - \bar{p}_{j+1/2}}{\Delta x} \right) + \frac{\varrho_j^{n+1} + \varrho_j^n}{2} g_j \right] \quad (\text{A3})$$

$$E_{H,j}^{n+1} = E_j^n + \frac{\Delta t^{n+1/2}}{a^{n+1/2}} \left[\frac{\left(\frac{1}{2}\bar{\varrho}_{j-1/2}\bar{v}_{j-1/2}^2 + \frac{\gamma}{\gamma-1}\bar{p}_{j-1/2} \right) \bar{v}_{j-1/2} - \left(\frac{1}{2}\bar{\varrho}_{j+1/2}\bar{v}_{j+1/2}^2 + \frac{\gamma}{\gamma-1}\bar{p}_{j+1/2} \right) \bar{v}_{j+1/2}}{\Delta x} \right] + \frac{\varrho_j^{n+1}v_j^{n+1} + \varrho_j^n v_j^n}{2} g_j \quad (\text{A4})$$

$$u_{H,j}^{n+1} = \frac{1}{\varrho_{H,j}^{n+1}} \left[\varrho_j^n u_j^n + \frac{\Delta t^{n+1/2}}{a^{n+1/2}} \left(\frac{\bar{\varrho}_{j-1/2}\bar{v}_{j-1/2}\bar{u}_{j-1/2} - \bar{\varrho}_{j+1/2}\bar{v}_{j+1/2}\bar{u}_{j+1/2}}{\Delta x} \right) \right]. \quad (\text{A5})$$

The quantity g_j is the time-centred value of the gravitational force averaged on the j -th cell calculated by expanding the density and acceleration fields and retaining all terms up to second-order in Δx :

$$g_j = \frac{1}{2a(t)\Delta x} \left[\phi_{j+1} - \phi_{j-1} + \frac{1}{12}(\phi_{j+1} - 2\phi_j + \phi_{j-1}) \frac{\delta \varrho_j}{\varrho_j} \right]. \quad (\text{A6})$$

The monotonicity of the numerical method is preserved by computing the density slope $\delta\varrho$ as:

$$\begin{aligned}\delta\varrho_j &= \tilde{\varrho}_{min} \text{sign}(\varrho_{j+1} - \varrho_{j-1}) \quad \text{if } (\varrho_{j+1} - \varrho_j)(\varrho_j - \varrho_{j-1}) < 0 \\ &= 0 \quad \text{otherwise ,}\end{aligned}\tag{A7}$$

where $\tilde{\varrho}_{min} = \min(|\varrho_{j+1} - \varrho_{j-1}|, 2|\varrho_j - \varrho_{j-1}|, 2|\varrho_{j+1} - \varrho_j|)$. Because of its smoothness, the gravitational potential does not require the same monotonicity constraint.

Points 2 and 3 are repeated for the other two orthogonal directions completing the three-dimensional hydrodynamical calculation.

4 – The hydrodynamical quantities are corrected by considering the expansion terms:

$$\varrho_j^{n+1} = \varrho_{H,j}^{n+1}\tag{A8}$$

$$v_j^{n+1} = \frac{2v_{H,j}^{n+1} - \Delta t^{n+1/2}(\dot{a}/a)^{n+1/2}v_j^n}{2 + \Delta t^{n+1/2}(\dot{a}/a)^{n+1/2}}\tag{A9}$$

$$E_j^{n+1} = \frac{E_{H,j}^{n+1} - \Delta t^{n+1/2}(\dot{a}/a)^{n+1/2}E_j^n}{1 + \Delta t^{n+1/2}(\dot{a}/a)^{n+1/2}}\tag{A10}$$

5 – Position and velocity of the N-body particles are updated by the two-step Lax–Wendroff scheme:
step 1

$$\mathbf{v}_{DM,j}^{n+1/2} = \mathbf{v}_{DM,j}^n - (\dot{a}^n \mathbf{v}_{DM,j}^n + \mathbf{g}_j^n) \frac{\Delta t^{n+1/2}}{2a^n}\tag{A11}$$

$$\mathbf{x}_{DM,j}^{n+1/2} = \mathbf{x}_{DM,j}^n + \mathbf{v}_{DM,j}^n \frac{\Delta t^{n+1/2}}{2a^n}\tag{A12}$$

step 2

$$\mathbf{v}_{DM,j}^{n+1} = \mathbf{v}_{DM,j}^n - \left(\dot{a}^{n+1/2} \mathbf{v}_{DM,j}^{n+1/2} + \mathbf{g}_j^{n+1/2} \right) \frac{\Delta t^{n+1/2}}{a^{n+1/2}}\tag{A13}$$

$$\mathbf{x}_{DM,j}^{n+1} = \mathbf{x}_{DM,j}^n + \mathbf{v}_{DM,j}^{n+1/2} \frac{\Delta t^{n+1/2}}{a^{n+1/2}}\tag{A14}$$

Here we indicate by \mathbf{g}_j^n the gravitational force on the j -th particle, computed by interpolating the values of the corresponding components at the eight neighbouring cells using the cloud-in-cell scheme.

6 – Energy is corrected to account for highly supersonic flows. We have introduced the internal energy equation. This is solved first including the flux term by the standard PPM integration procedure:

$$\tilde{e}_{H,j}^{n+1} = e_j^n + \frac{\Delta t^{n+1/2}}{a(t^{n+1/2})} \left(\frac{\bar{p}_{j-1/2} \bar{v}_{j-1/2} - \bar{p}_{j+1/2} \bar{v}_{j+1/2}}{(\gamma - 1) \Delta x} \right) .\tag{A15}$$

Then this value is corrected as:

$$e_{H,j}^{n+1} = \tilde{e}_{H,j}^{n+1} + \frac{1}{a^{n+1/2}} \frac{\Delta t^{n+1/2}}{\Delta x} \frac{p_j^{n+1/2}}{\varrho_j^n} (\bar{v}_{j-1/2} - \bar{v}_{j+1/2}) ,\tag{A16}$$

where $p_j^{n+1/2} = (\bar{p}_{j-1/2} + \bar{p}_{j+1/2})/2$. Finally, we consider also the expansion term in the internal energy equation:

$$e_j^{n+1} = \frac{e_{H,j}^{n+1} - \Delta t^{n+1/2}(\dot{a}/a)^{n+1/2}e_j^n}{1 + \Delta t^{n+1/2}(\dot{a}/a)^{n+1/2}} .\tag{A17}$$

The internal energy is used if conditions (27) hold:

$$\sum_{i=1,3} \frac{\partial v_j}{\partial x_j} \geq 0 ; \quad \frac{1}{p_j} \left[\sum_{i=1,3} \left(\frac{\partial p_i}{\partial x_i} \right)^2 \right]^{1/2} \leq \eta_1 \quad j=1,3.\tag{A18}$$

If neither of these conditions are verified, internal energy is computed according to expression (28):

$$e_j = \begin{cases} E_j - \frac{1}{2} \varrho_j \mathbf{v}^2 & \text{if } E_j - \frac{1}{2} \varrho_j \mathbf{v}^2 / \max(E_{j-1}, E_j, E_{j+1}) \geq \eta_2 \\ e_j & \text{otherwise .} \end{cases}\tag{A19}$$

Note that as we are dealing with errors that can be advected with the total energy calculation, we have to consider not just the j -th cell but also its neighbourhood (that in one dimension comprises the two zones $j \pm 1$).

APPENDIX B: CALCULATING FLUXES

Here we describe briefly the procedure used to calculate the time averaged values of the hydrodynamical quantities at the zone interfaces $\bar{q}_{j+1/2}$, $\bar{p}_{j+1/2}$, $\bar{v}_{j+1/2}$ and $\bar{u}_{j+1/2}$. We include to second-order both the gravity and the cosmic expansion, which enter the characteristic equations as described in Section 3.2.

We indicate by $w(x)$ the interpolated piecewise continuous function representing the generic hydrodynamical variable. The quantity w_j represents the mean value of $w(x)$ over the j -th zone.

We define $\tilde{w}_{j+1/2,L}$ and $\tilde{w}_{j+1/2,R}$, first approximations to the effective left and right states of the Riemann problem, as:

$$\tilde{w}_{j+1/2,L} = f_{j+1/2,L}(x_{j+1/2} - \tilde{x}_{j+1/2,L}), \quad (B1)$$

$$\tilde{w}_{j+1/2,R} = f_{j+1/2,R}(-x_{j+1/2} + \tilde{x}_{j+1/2,R}), \quad (B2)$$

where

$$f_{j+1/2,L}(\Delta x) = \frac{1}{\Delta x} \int_{x_{j+1/2}-\Delta x}^{x_{j+1/2}} w(\xi) d\xi, \quad f_{j+1/2,R}(\Delta x) = \frac{1}{\Delta x} \int_{x_{j+1/2}}^{x_{j+1/2}+\Delta x} w(\xi) d\xi, \quad (B3)$$

$$\tilde{x}_{j+1/2,L} = x_{j+1/2} - \max(0, \Delta t^{n+1/2} \lambda_{j,+}), \quad \tilde{x}_{j+1/2,R} = x_{j+1/2} + \max(0, -\Delta t^{n+1/2} \lambda_{j+1,-}) \quad (B4)$$

and

$$\lambda_{j,+} = \frac{v_j^n + c_j^n}{a^n}, \quad \lambda_{j+1,-} = \frac{v_{j+1}^n - c_{j+1}^n}{a^n}. \quad (B5)$$

We correct our initial guess for the left and right states by solving the equations of gas dynamics in characteristic form (see Section 3.2). First we calculate the mean value of the hydrodynamic variables in the domains defined by each of the characteristic lines coming from the left and the right of the zone boundary $j + 1/2$:

$$w_{j+1/2,L}^k = f_{j+1/2,L}(x_{j+1/2} - x_{j+1/2,L}^k), \quad (B6)$$

$$w_{j+1/2,R}^k = f_{j+1/2,R}(-x_{j+1/2} + x_{j+1/2,R}^k), \quad (B7)$$

where $k = +, 0, -$ and

$$x_{j+1/2,L}^k = x_{j+1/2} - \Delta t \lambda_{j,k}, \quad x_{j+1/2,R}^k = x_{j+1/2} - \Delta t \lambda_{j+1,k}. \quad (B8)$$

Then we correct the initial guess considering only that information which can reach the zone edge during the current timestep:

$$p_{j+1/2,S} = \bar{p}_{j+1/2,S} + \tilde{C}_{j+1/2,S}^2 (\beta_{j+1/2,S}^+ + \beta_{j+1/2,S}^-), \quad (B9)$$

$$v_{j+1/2,S} = \bar{v}_{j+1/2,S} + \tilde{C}_{j+1/2,S} (\beta_{j+1/2,S}^+ - \beta_{j+1/2,S}^-), \quad (B10)$$

$$\varrho_{j+1/2,S} = \left(\frac{1}{\bar{\varrho}_{j+1/2,S}} - \sum_{k=+,0,-} \beta_{j+1/2,S}^k \right)^{-1}. \quad (B11)$$

Here $\tilde{C}_{j+1/2,S}^2 = \gamma \bar{p}_{j+1/2} \bar{\varrho}_{j+1/2}$ and $S = L, R$. We also have

$$u_{j+1/2,L} = \bar{u}_{j+1/2,L}, \quad \beta_{j+1/2,L}^k = 0 \quad \text{if} \quad \lambda_{j,k} \leq 0, \quad (B12)$$

$$u_{j+1/2,R} = \bar{u}_{j+1/2,R}, \quad \beta_{j+1/2,R}^k = 0 \quad \text{if} \quad \lambda_{j+1,k} \leq 0. \quad (B13)$$

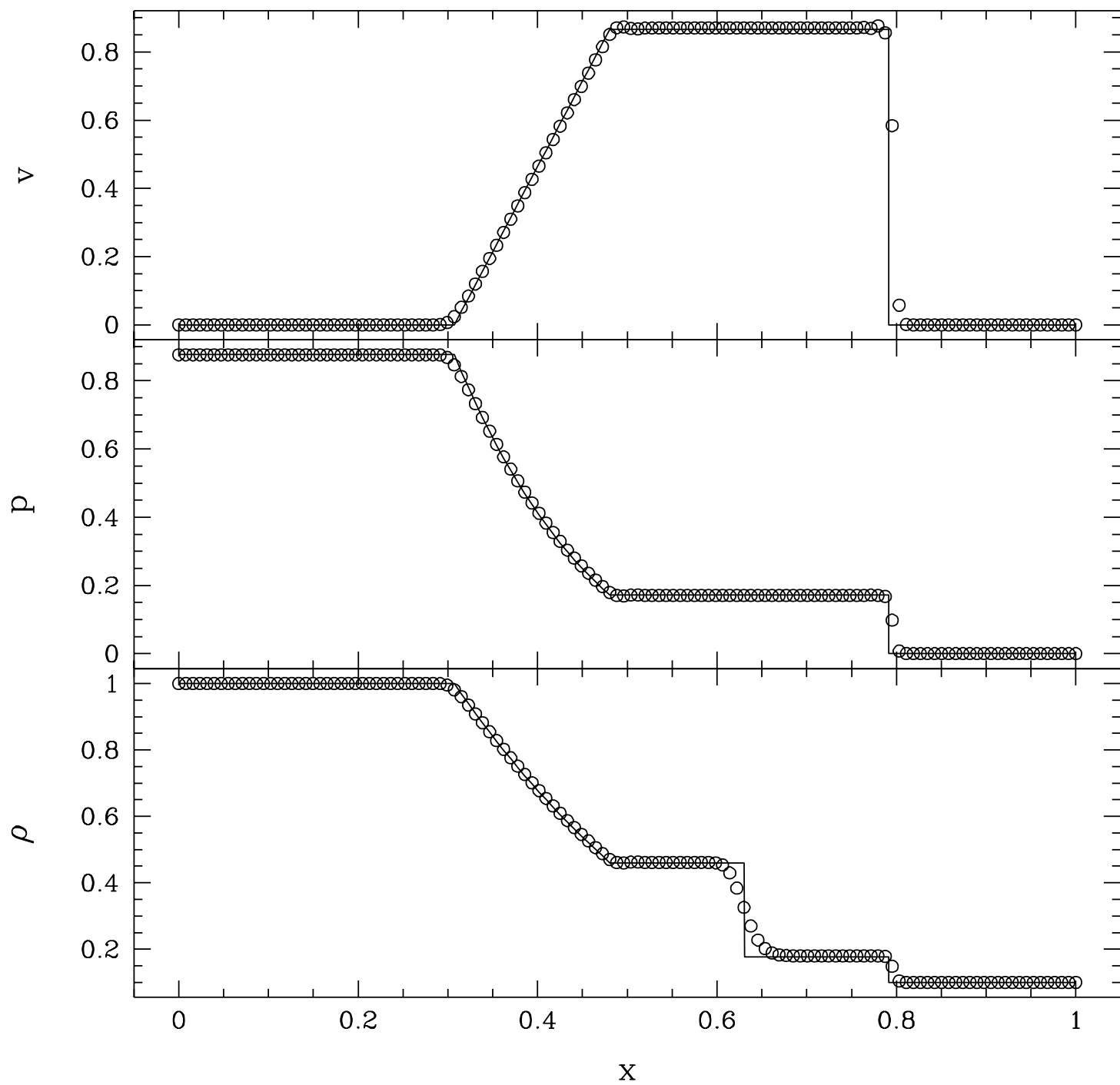
Otherwise

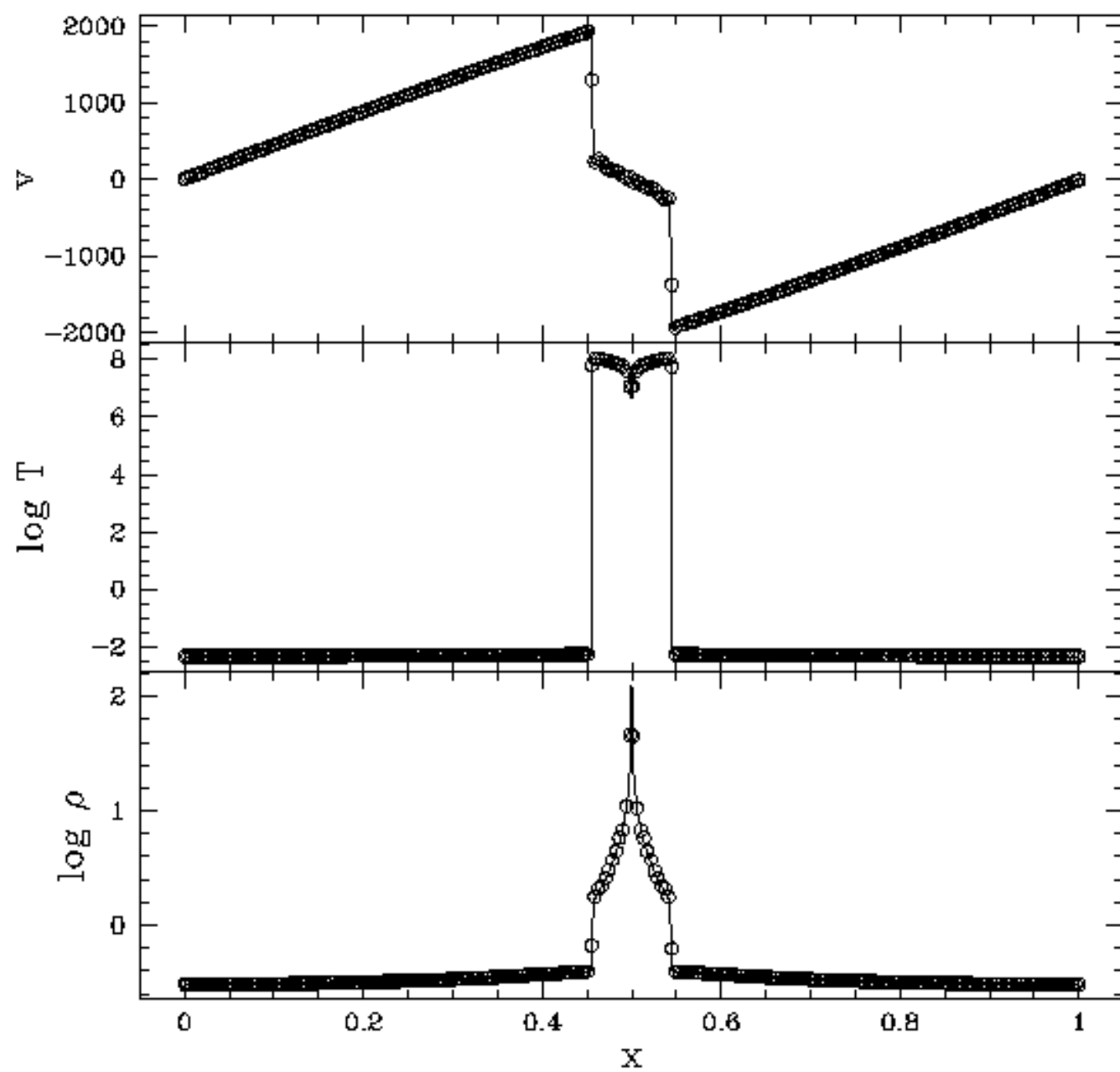
$$\beta_{j+1/2,S}^\pm = \mp \frac{1}{\tilde{C}_{j+1/2,S}} \left[(\bar{v}_{j+1/2,S} - v_{j+1/2,S}^\pm) \pm \frac{\bar{p}_{j+1/2,S} - p_{j+1/2,S}^\pm}{\tilde{C}_{j+1/2,S}} \pm \Delta t \left(2 \frac{\dot{a}}{a} \frac{p_{j+1/2,S}^\pm}{\tilde{C}_{j+1/2,S}} \pm \frac{\dot{a}}{a} v_{j+1/2,S}^\pm \mp g_{j+1/2,S}^\pm \right) \right] \quad (B14)$$

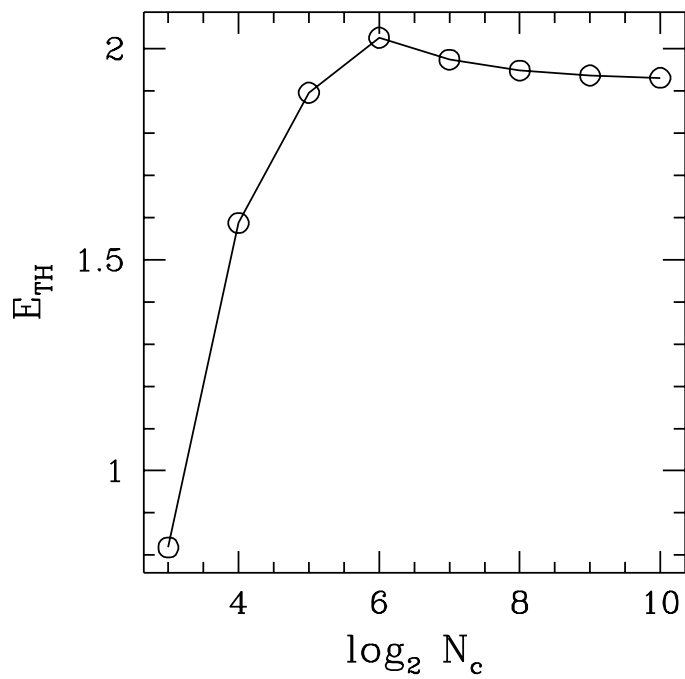
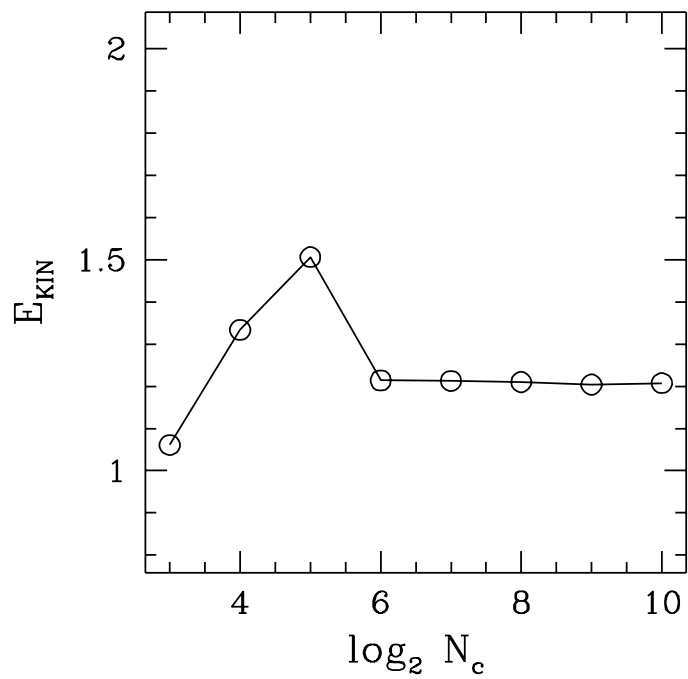
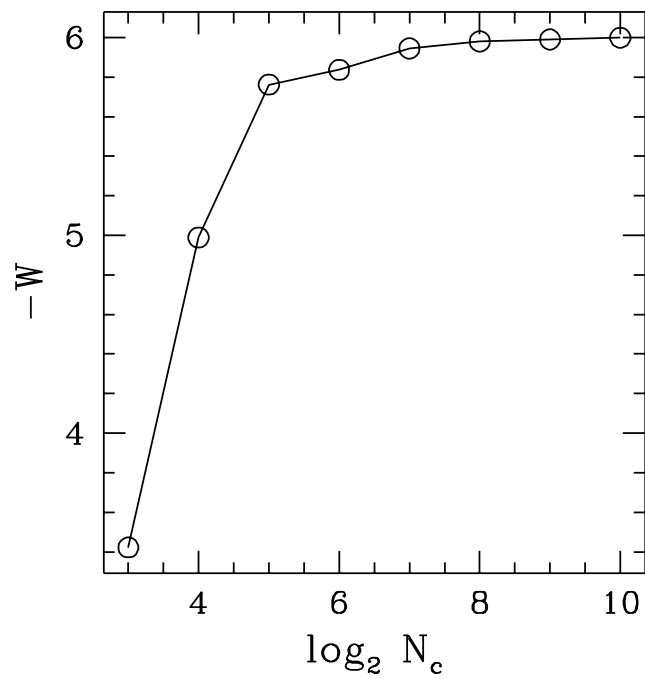
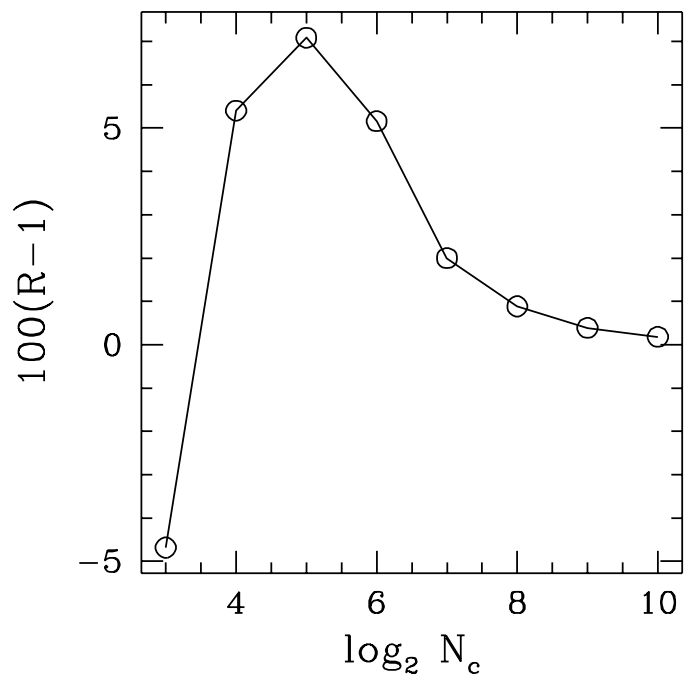
$$\beta_{j+1/2,S}^0 = \left(\frac{\bar{p}_{j+1/2,S} - p_{j+1/2,S}^0}{\tilde{C}_{j+1/2,S}^2} + \frac{1}{\bar{\varrho}_{j+1/2,S}} - \frac{1}{\varrho_{j+1/2,S}^0} + 2 \frac{\dot{a}}{a} \frac{p_{j+1/2,S}^\pm}{\tilde{C}_{j+1/2,S}^2} \right) \quad (B15)$$

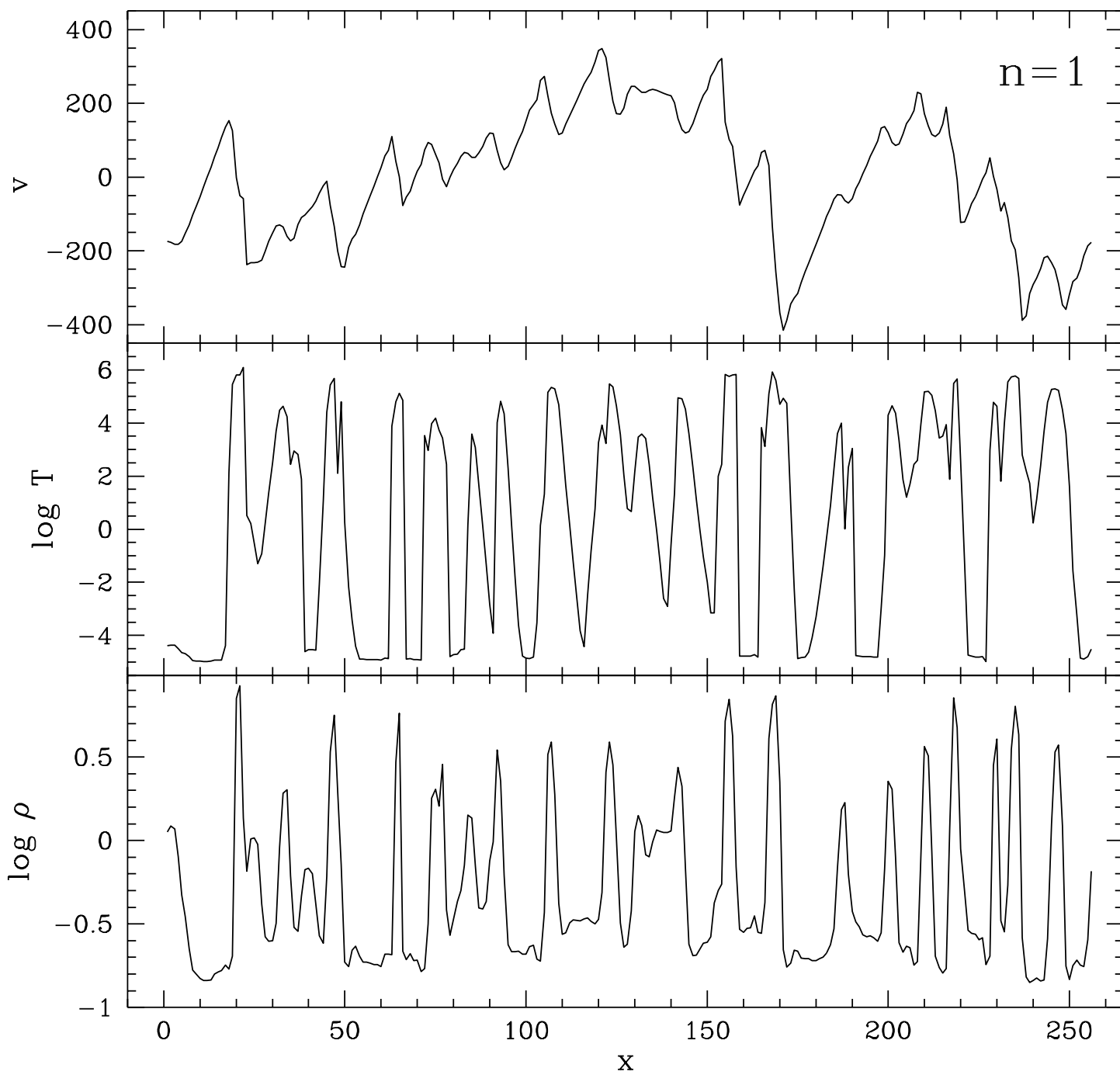
$$u_{j+1/2,S} = u_{j+1/2,S}^0. \quad (B16)$$

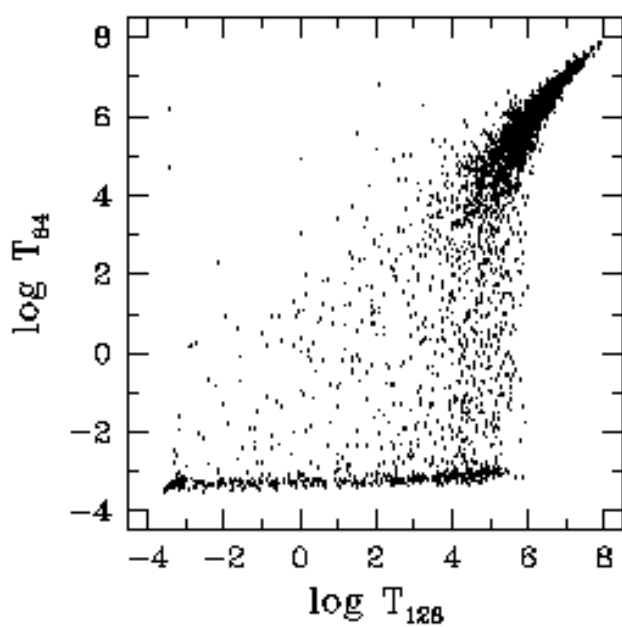
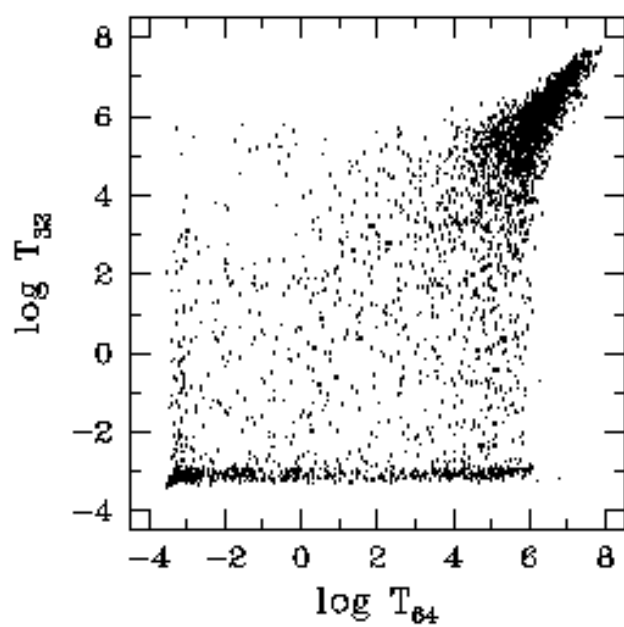
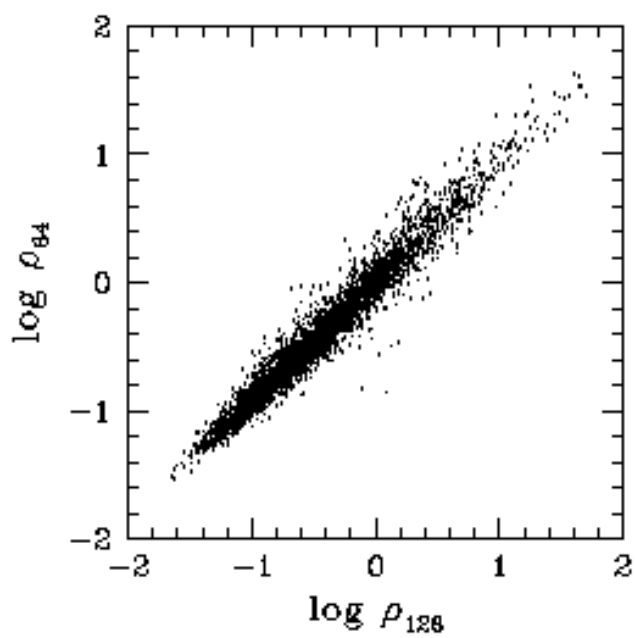
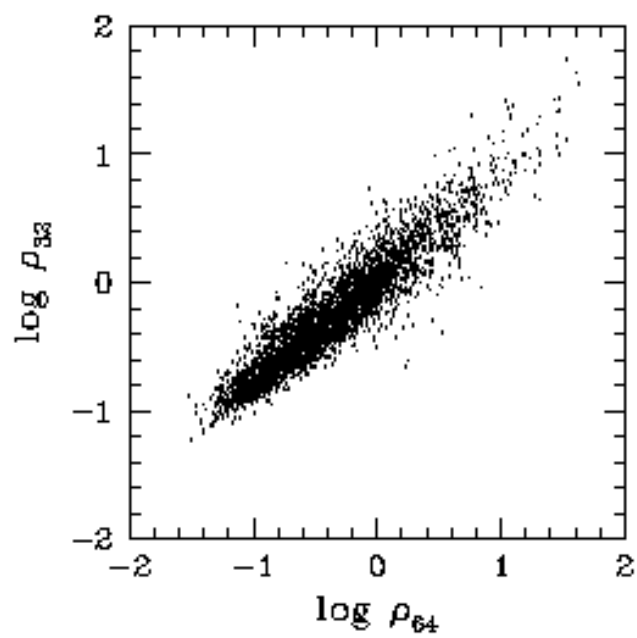
The time averaged estimates of the solution at $x_{j+1/2}$ are determined by calculating the non-linear interaction of the left and right states calculated in equations (A33)–(A35). This interaction is described by the solution to the Riemann problem with these left and right states as initial conditions. The Riemann problem is solved in a standard way, as described by Van Leer (1979) and Gottlieb & Groth (1988).

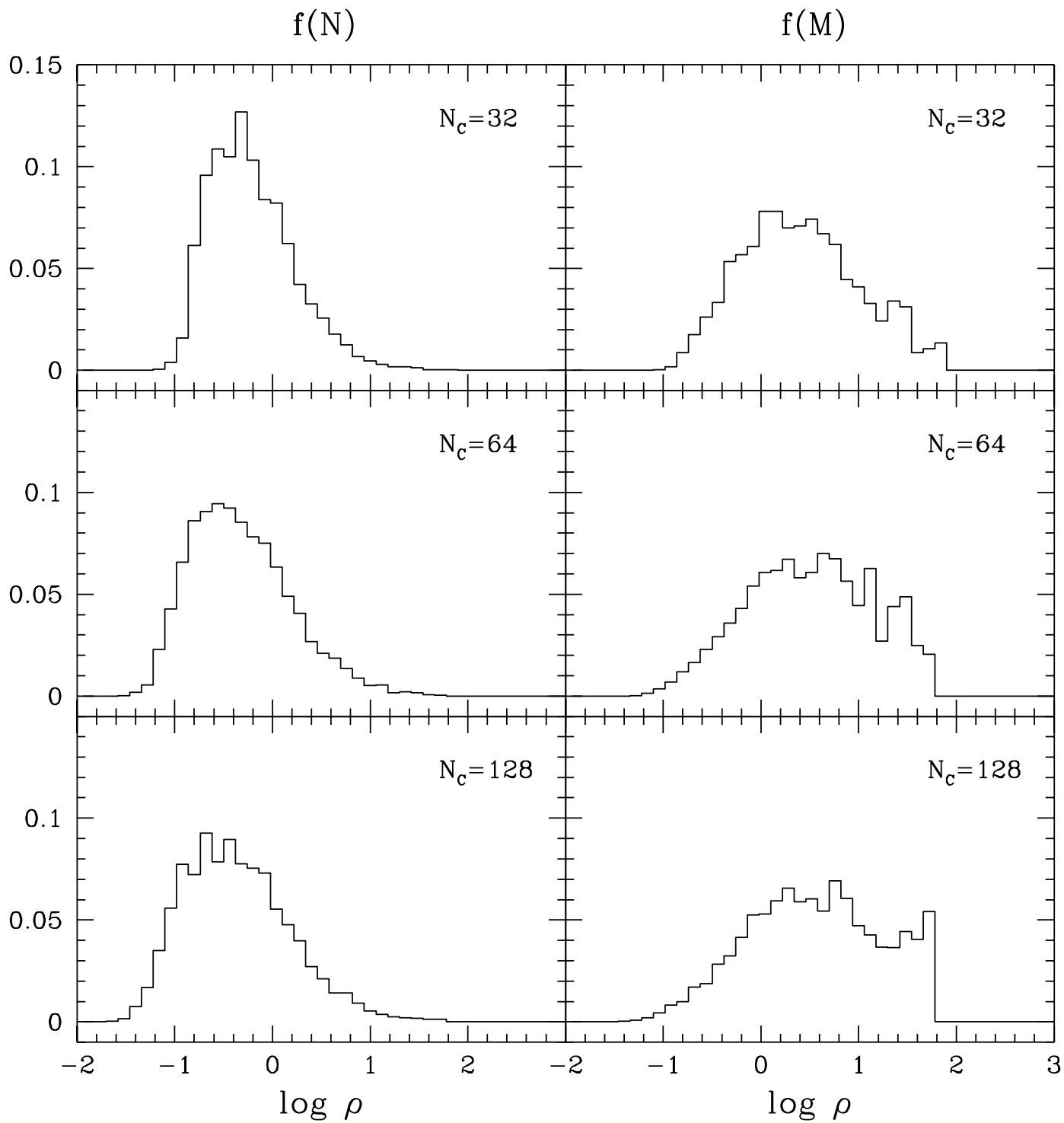


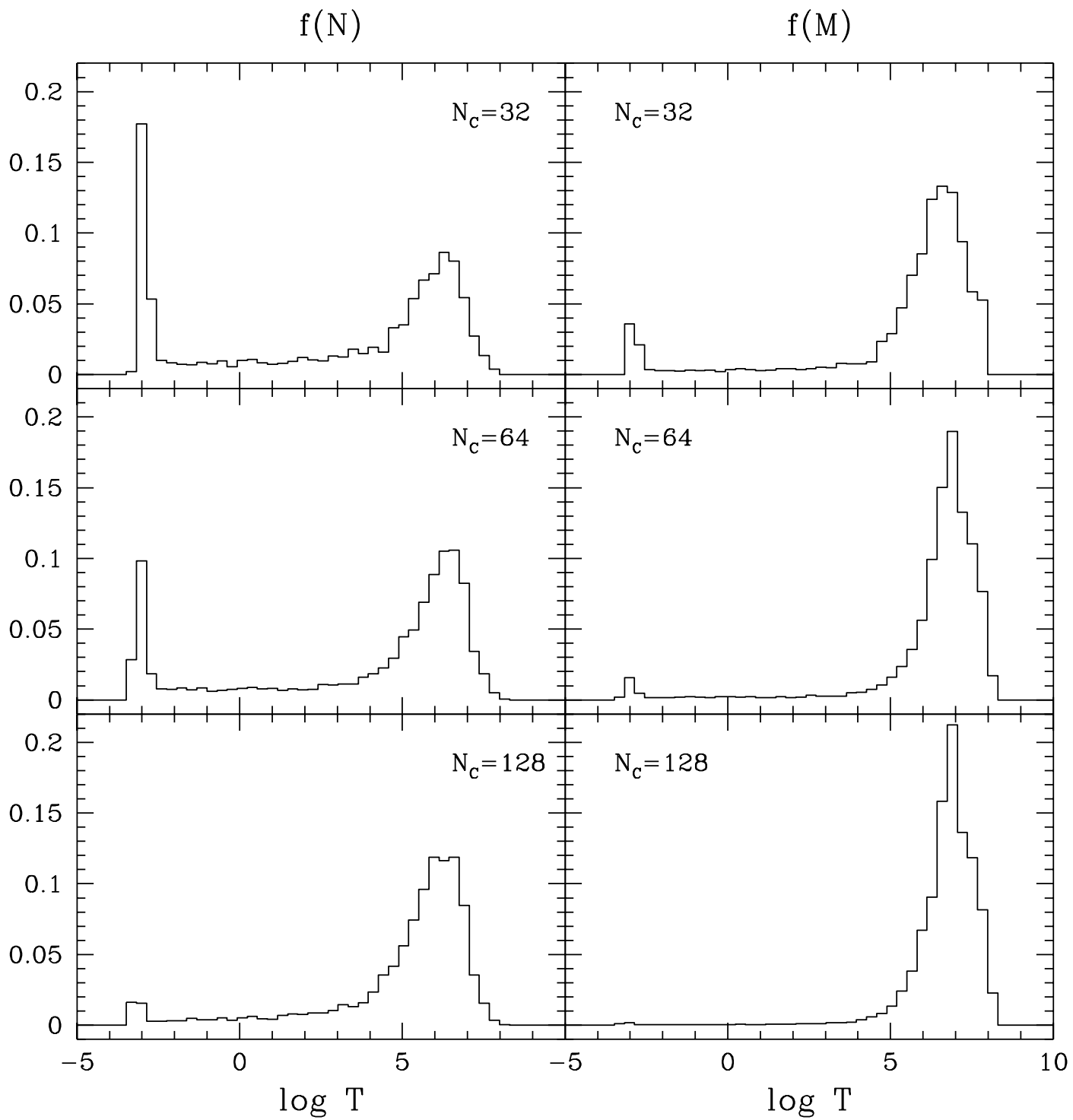


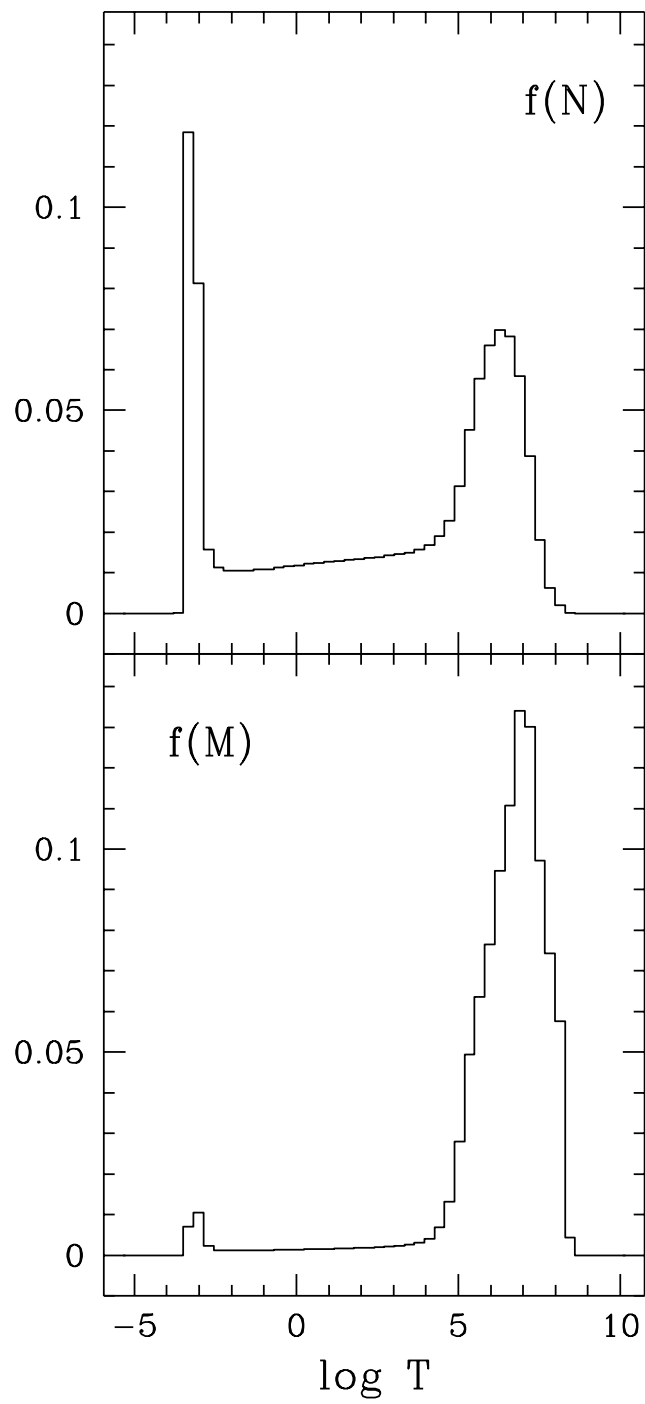
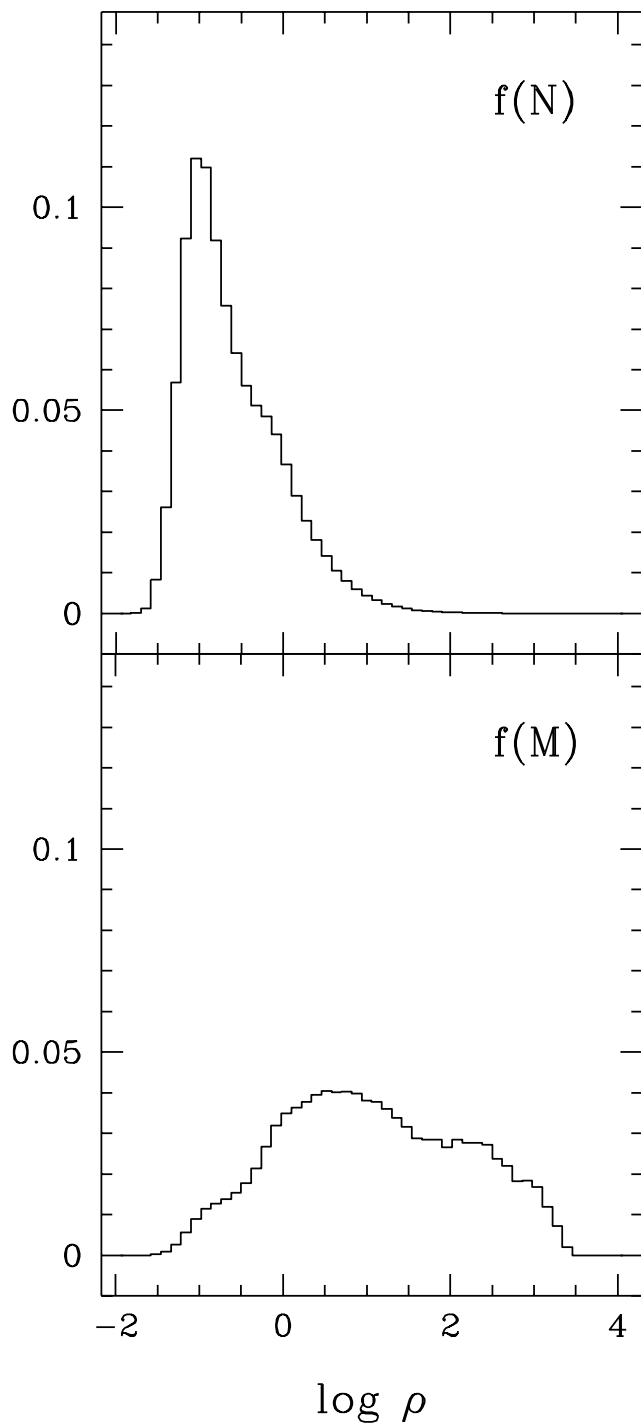












This figure "fig09.gif" is available in "gif" format from:

<http://arXiv.org/ps/astro-ph/9701170v1>

